Optics Letters

High-order orbital angular momentum mode generator based on twisted photonic crystal fiber

CAILING FU,[1] SHEN LIU,[1] YING WANG,[1] ZHIYONG BAI,[1] JUN HE,[1] CHANGRUI LIAO,[1] YAN ZHANG,[1] FENG ZHANG,[1] BIN YU,[1] SHECHENG GAO,[2] ZHAOHUI LI,[3] AND YIPING WANG[1,*]

[1]Key Laboratory of Optoelectronic Devices and Systems of Ministry of Education and Guangdong Province, College of Optoelectronic Engineering, Shenzhen University, Shenzhen 518060, China
[2]China Department of Electronic Engineering, Jinan University, Guangzhou 510632, China
[3]State Key Laboratory of Optoelectronic Materials and Technologies and School of Electronics and Information Technology, Sun Yat-sen University, Guangzhou 510275, China
*Corresponding author: ypwang@szu.edu.cn

Received 17 January 2018; revised 8 March 2018; accepted 13 March 2018; posted 16 March 2018 (Doc. ID 319689); published 10 April 2018

High-order orbital angular momentum (OAM) modes, namely, OAM_{+5} and OAM_{+6}, were generated and demonstrated experimentally by twisting a solid-core hexagonal photonic crystal fiber (PCF) during hydrogen–oxygen flame heating. Leaky orbital resonances in the cladding depend strongly on the twist rate and length of the helical PCF. Moreover, the generated high-order OAM mode could be a polarized mode. The secret of the successful observation of high-order modes is that leaky orbital resonances in the twisted PCF cladding have a high coupling efficiency of more than −20 dB.

OCIS codes: (050.4865) Optical vortices; (060.2340) Fiber optics components; (060.2330) Fiber optics communications; (060.4230) Multiplexing.

https://doi.org/10.1364/OL.43.001786

The optical orbital angular momentum (OAM) of a light beam has exhibited potential applications in optical communications [1], optical tweezers [2], and atom manipulation [3]. Existing ways to generate OAM modes are usually based on free-space coupling methods, such as cylindrical-lens mode converters [4], spatial light modulators [5], integrated silicon devices [6], and micrometer-scale metamaterials [7]. Researchers have recently demonstrated various all-fiber OAM generators based on standard single-mode fibers (SMFs) [8], few-mode fibers [9–15], photonic crystal fibers (PCFs) [16,17], and other special types of fibers [18,19]. For example, the authors recently reported on an OAM convertor based on a helical long-period fiber grating inscribed by means of twisting a standard SMF [8]. A few researchers have demonstrated OAM_{+1} and OAM_{+2} convertors based on two- [9–11] and four-mode fibers [12–15], respectively. Moreover, Wong *et al.* demonstrated, for the first time, excitation of OAM resonances in a helically twisted standard solid-core hexagonal PCF, but no OAM modes were experimentally observed in such a twisted PCF [16]. $OAM_{\pm 1}$ modes have been demonstrated in a special type of twisted PCF, namely, a three-bladed core PCF [17]. In-fiber high-order OAM generators could be used to achieve a higher data transmission capacity in an all-fiber optical communication system. Unfortunately, no third- or higher-order modes have yet been experimentally demonstrated by in-fiber OAM generators.

In this Letter, OAM_{+6} modes are experimentally demonstrated by use of a helically twisted PCF. Such a high-order OAM generator was fabricated by twisting a solid-core hexagonal PCF during hydrogen–oxygen flame heating. The dependence of leaky cladding orbital resonance on the twist rate and length of the helical PCF was investigated to achieve a high-quality, high-order OAM generator. Moreover, experimental results exhibit that the generated OAM_{+6} mode could be a polarized mode.

The experimental setup illustrated in Fig. 1 in [8] and an endlessly single-mode solid-core PCF (ESM-12, NKT Photonics, Denmark) were employed to fabricate a helical PCF. As shown in Fig. 1, the employed PCF exhibits a hexagonal microstructure with an air-hole diameter of 3.6 μm and a hole-to-hole space of 7.9 μm. One end of the PCF was fixed on a translation stage1. Another end of the PCF was installed along the central axis of a high-speed rotation motor affixed on another translation stage2. A hydrogen-oxygen flame produced by a hydrogen generator was launched to heat the PCF. The left end of the PCF was twisted via the motor with a rotational speed of Ω while its two ends continuously moved along the fiber axis with a velocity of $v_1 = 1.60$ mm/s and $v_2 = 1.38$ mm/s via translation stage1 and translation stage2, respectively. Note that the length (L) of the twisted PCF is given by the equation $L = v_1 * T$, the twist rate (α) is given by the equation $\alpha = \pi\Omega/(30v_1)$, and the helical pitch (Λ) is given by the equation $\Lambda = 60\ v_1/\Omega$. After twisting the fiber with a rotational speed of $\Omega = 115$ rpm, as shown in Fig. 1(b), a helical PCF with a twist rate of 7.53 rad/mm (helical pitch: 834.78 μm) was achieved. It is interesting to see from Figs. 1(c) and 1(d) that the diameter of the PCF was shortened from 125 to 109 μm, due to the heat-induced shrinking of air holes.

Two ends of the achieved helical PCF with a length of 4.6 mm and a twist rate of 7.53 rad/mm were spliced with

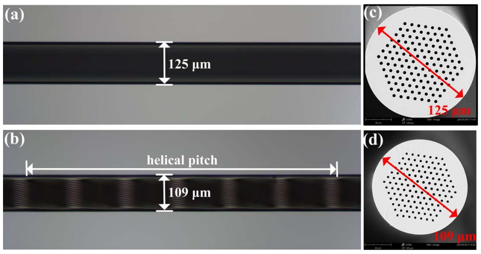

Fig. 1. Side-view microscope images of the (a) untwisted and (b) twisted PCFs; scanning electron micrographs of the (c) untwisted and (d) twisted PCF cross sections with hexagonal air-hole microstructure.

two standard SMFs, respectively, to measure its transmission spectrum using an optical spectrum analyzer (Model AQ6370C) and an amplified spontaneous emission broadband light source with a wavelength range from 1250 to 1670 nm. As shown in Fig. 2(a), two resonance dips, Dip_1 (1275.52 nm, −8.25 dB) and Dip_2 (1501.36 nm, −8.82 dB), were observed in the transmission spectrum, illustrated by the bold blue curve. A hexagonal cladding structure in the untwisted PCF cladding supports a fundamental "space-filling" mode (SM) whose axial Poynting vector points precisely along the fiber axis. When the PCF is gently twisted ($\alpha\Lambda \ll 1$), this SM is forced to follow a helical trajectory around the fiber core. This leads to a component of momentum flow in the azimuthal direction, creating discrete OAMs and causing orbital resonances [16,17]. As a result, leaky orbital resonances in the cladding induce a series of dips in the transmission spectrum, as shown in Fig. 2.

To investigate the effect of the twisted length on the transmission spectrum, the helical PCF sample shown previously was cut repeatedly to reduce its length from 4.6 to 1.8 mm using a computer-controlled precision cleaving system comprising an optical fiber cleaver, an industrial CCD camera, and a precision translation stage. In our experiments, the helical PCF was gradually cut 16 times to observe its transmission spectrum evolution with the decrease of the fiber length, as shown in the inset of Fig. 2. The peak attenuation error of Dip_1 and Dip_2 in the helical PCF maybe result from the length error of the helical PCF cut by the cleaving system. For clarity, Fig. 2 shows only eight transmission spectrum curves. For each resonance dip (Dip_1 and Dip_2), as shown in Fig. 2, the leaky orbital resonance strength in the cladding increased and then decreased gradually as the helical PCF length decreased [20,21]. In other words, the helical PCF has an optimum length, corresponding to the maximum coupling attenuation at the resonant wavelength, which is similar to that reported on page 37 in [22]. For example, Dip_2 exhibited the maximum coupling attenuation of −17.43 dB at the wavelength of 1498.35 nm when the helical PCF length was shortened to 4.4 mm, as illustrated by the bold black curve in Fig. 2. In contrast, Dip_1 exhibited the maximum coupling attenuation of −28.18 dB at the wavelength of 1276.70 nm when the helical PCF length was shortened to 3.4 mm, as illustrated by the bold pink curve in Fig. 2. Therefore, leaky orbital resonances in the cladding depend strongly on the length of the twisted PCF.

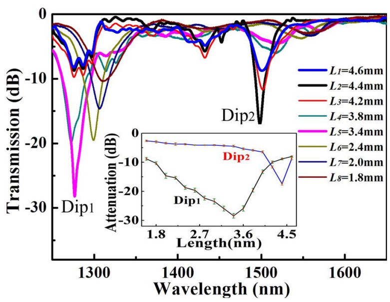

Fig. 2. Transmission spectrum evolution of the helical PCF with the decrease of the fiber length from 4.6 to 1.8 mm. Inset: attenuation at the resonant wavelengths of Dip_1 and Dip_2 versus the length of the helical PCF.

To investigate the effect of the twist rate on the resonant wavelength, six helical PCF samples, with twist rates of 7.53, 7.85, 8.18, 8.51, 8.84, and 9.16 rad/mm, were fabricated by applying rotational speeds of 115, 120, 125, 130, 135, and 140 rpm, respectively, to the rotation motor. For each helical PCF sample, as shown in Fig. 3(a), one or two leaky orbital resonance dips, Dip_1 and Dip_2, were observed within the wavelength range from 1250 to 1670 nm. For each order OAM mode, the resonant wavelength, corresponding to Dip_1 or Dip_2, increases linearly with the twist rate, as shown in Fig. 3(b). The resonant wavelength error of Dip_1 and Dip_2 maybe results from the helical pitch error of the twisted PCF. This is in good agreement with previously reported results [16]. According to the orbital resonance condition, the resonant wavelength (λ_R) of the helical PCF can be given by

$$\lambda_R = 2\pi n_{\mathrm{SM}}\rho^2\alpha/|l|, \tag{1}$$

where ρ is the radius of the cladding resonance, l is an integer representing its order, and n_{SM} is the refractive index corresponding to the SM mode. Although it is difficult to assign precise values to n_{SM} and ρ^2 in advance, experimental results reveal that the product $n_{\mathrm{SM}}\rho^2$ is a constant for a given PCF [16]. According to Eq. (1) and the experimental data shown in Fig. 3(b), the reciprocal resonant wavelength (λ), in units of μm^{-1}, was plotted against mode order, which demonstrates that

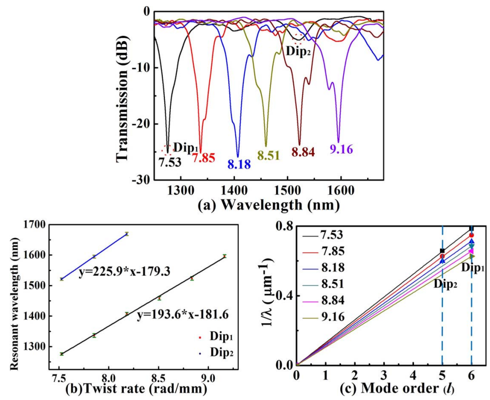

Fig. 3. (a) Transmission spectra of six helical PCF samples with a twist rate of 7.53, 7.85, 8.18, 8.51, 8.84, and 9.16 rad/mm, respectively; (b) resonant wavelengths of Dip_1 and Dip_2 versus the twist rate; (c) reciprocal resonant wavelength (λ_R) in units of at μm^{-1} plotted against mode order for the experimental data illustrated in (b). Note that Dip_2 of the three twisted PCF samples, with higher twist rates of 8.51, 8.84, and 9.16 rad/mm, respectively, were not observed due to the limit of the wavelength measurement range.

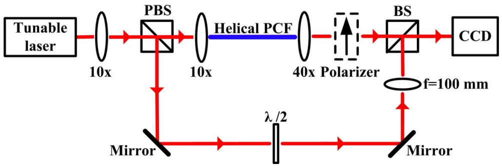

Fig. 4. Schematic diagram of experimental setup for detecting OAM modes generated by the helical PCF. PBS: polarized beam-splitter; BS: beamsplitter.

the orders of successive cladding resonances run from $l = 5$ to $l = 6$. That is, the resonance dips, Dip_1 and Dip_2, as illustrated in Fig. 3(a), correspond to the OAM_{+6} and OAM_{+5} mode, respectively, generated by the helical PCF.

An experimental setup was demonstrated to detect the OAM modes generated by the helical PCFs, as shown in Fig. 4. Light from a tunable laser (Model 81940A) with a wavelength range from 1520 to 1620 nm was collimated into a tunable polarized beam splitter (PBS) through a 10× objective lens to divide it into two parts. One part of the light was coupled into a helical PCF sample through a 10× objective lens to generate OAM modes, and then collimated into a beamsplitter (BS) through a 40× objective lens and a polarizer. Another part of the light was propagated into a half-wave plate and then into a BS through a lens with a focal length of 100 mm as a reference beam. The OAM modes generated by the helical PCF interfered with the reference beam on the BS. The beam profile and interference pattern of the generated OAM were observed using an infrared camera (Model 7290A). The splitting ratio of the PBS can be tuned to improve the interference pattern on the BS.

As shown in Fig. 5(a), a helical PCF sample with a twist rate of 9.10 rad/mm and a length of 2.30 mm was fabricated to observe the generated OAM modes. Its transmission spectrum exhibits a resonance dip with a maximum attenuation of −22.27 dB at the resonant wavelength of 1578.62 nm. As shown in Fig. 5(f), the beam profile of the helical PCF at the nonresonant wavelength of 1521.62 nm exhibits a very high intensity in the core. In contrast, as shown in Fig. 5(c), the beam profile of the helical PCF at the resonant wavelength of 1578.60 nm exhibits a very low intensity in the core. This indicates that the fundamental core mode is coupled into leaky OAM cladding modes, resulting from leaky orbital resonance. By establishing a two-dimensional numerical model in a helicoidal coordinate system [16], we calculated the beam profile of the helical PCF with finite element modeling. As shown in Figs. 5(b), 5(c), 5(e), and 5(f), the simulated beam profile of the helical PCF is in good agreement with the measured beam profile whether at the resonant or nonresonant wavelength.

To verify the characteristics of a helical phase, the generated OAM mode was interfered with the reference beam. Consequently, anticlockwise spiral interference patterns for the OAM_{+6} mode, as shown in Fig. 5(d), were clearly observed at a resonant wavelength of 1578.62 nm, which demonstrates that the OAM_{+6} mode was successfully generated. This is in good agreement with a previously reported simulation result, where an N-order ($N = 6$) OAM mode can be generated by the PCF with N-fold ($N = 6$) rotational symmetry in the cross section [23]. It is well known that the OAM of light was excited at the output of the twisted PCF, resulting from the twist-induced helical structure in the fiber. It is interesting to find from Fig. 5(g) that a weak OAM_{+6} mode was also observed at the nonresonant wavelength of 1521.62 nm. This indicates that the fundamental core mode could be coupled into leaky OAM cladding modes within a wide wavelength range. And a high-quality OAM_{+6} mode occurred at the resonant wavelength with a high coupling efficiency of −22.27 dB. Moreover, our experiments show that the higher the coupling efficiency of the resonance dip is, the easier it is to observe high-quality OAM modes. Compared with a high coupling efficiency of more than −20 dB in our helical PCF samples, the maximum coupling efficiency is only about −5 dB in the helical PCF samples reported by Xi *et al.* in [17], which may be why no OAM modes were experimentally observed.

The beam profiles and interference patterns of the OAM_{+6} mode generated by the helical PCF at the resonant wavelength of 1578.60 nm were recorded by adjusting the polarizer in Fig. 4 to polarization orientations of 0°, 45°, 90°, and 135°. As shown in Fig. 6, both the beam profile and interference pattern of the OAM_{+6} mode depend strongly on the polarization state of the light. Therefore, the generated OAM_{+6} mode could be a polarized mode [24]. Furthermore, a tunable laser, a polarization synthesizer (Agilent Model N7786B), and an optical power meter (Agilent Model N7744A) were employed to

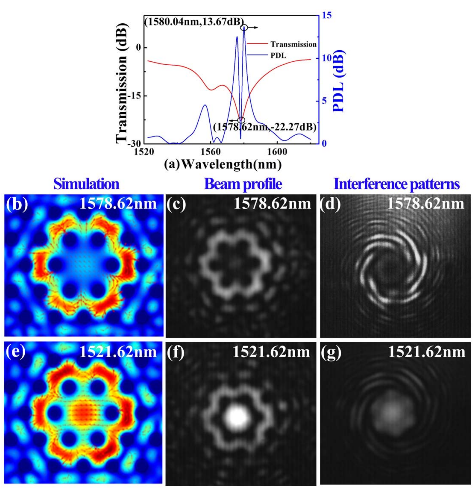

Fig. 5. (a) Transmission spectrum and PDL of the helical PCF; (b) and (e) simulated beam profiles, (c) and (f) measured beam profiles, and (d), (g) measured interference patterns of the OAM_{+6} mode generated by the helical PCF at the resonant wavelength of (b), (c), (d), 1578.62 nm and the nonresonant wavelength of (e), (f), (g) 1521.62 nm.

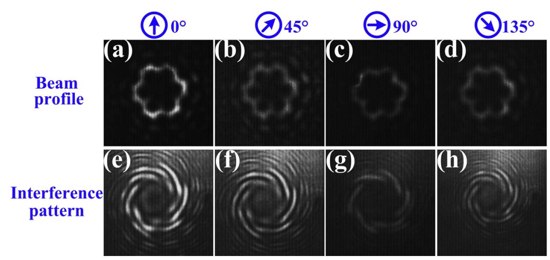

Fig. 6. Beam profiles (upper) and interference patterns (lower) of the OAM_{+6} mode generated by the helical PCF at the resonant wavelength of 1578.60 nm at the polarization states of (a), (e) 0°; (b), (f) 45°; (c), (g) 90°; and (d), (h) 135°.

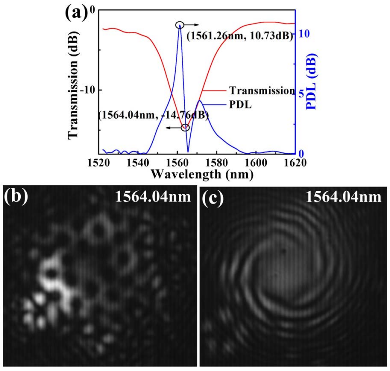

Fig. 7. (a) Transmission spectrum and PDL of the helical PCF; (b) beam profile; and (c) interference pattern of the OAM_{+5} mode generated by the helical PCF at the wavelength of 1564.04 nm.

measure its polarization-dependent loss (PDL). As shown in Fig. 5(b), the helical PCF has a maximum PDL of up to 13.67 dB at the wavelength of 1580.04 nm, which is due to an asymmetric azimuthal profile of refractive index modulation, resulting from the twist-induced deviations of the hexagonal microstructure, in the fiber. Therefore, such a helical PCF could be a polarization-dependent device. We will build a free-space polarization analysis system to investigate further the polarization dependence of the twisted PCF in the future.

In Fig. 3(c), Dip_2 indicates that the OAM_{+5} could be generated in the helical PCF. As shown in Fig. 2, leaky orbital resonances in the cladding depend strongly on the length of the helical PCF, and it is impossible that Dip_1 and Dip_2 simultaneously realize the maximum coupling attenuation by improving the length of the twisted PCF. So, another helical PCF sample was fabricated by applying a smaller twist rate of 7.72 rad/mm to bring Dip_2 within the wavelength range (1520–1620 nm) of our tunable laser and by improving its length to 2.72 mm to achieve the maximum attenuation of −14.76 dB, as shown in Fig. 7(a). The maximum PDL of the helical PCF sample is 10.73 dB. As shown in Figs. 7(b) and 7(c), we measured the beam profile and interference pattern corresponding to the leaky orbital resonance, namely, Dip_2, of the helical PCF, using the experimental setup illustrated in Fig. 4. The anticlockwise spiral interference patterns for the fifth-order OAM mode were clearly observed at a resonant wavelength of 1564.04 nm, as shown in Fig. 7(c). This demonstrates that the OAM_{+5} mode was successfully generated.

In conclusion, we generated and observed experimentally high-order OAM modes, namely, OAM_{+5} and OAM_{+6}, by twisting a solid-core hexagonal PCF during hydrogen–oxygen flame heating. Leaky orbital resonances in the cladding depend strongly on the twist rate and length of the helical PCF. Moreover, the generated high-order OAM mode could be a polarized OAM mode. The secret of the successful observation of high-order modes is that leaky orbital resonances in the twisted PCF cladding have a high coupling efficiency that exceeds −20 dB. Such a high-order OAM generator could be used to enhance data-transmission capacity in all-fiber optical communication systems.

Funding. National Natural Science Foundation of China (NSFC) (61425007, 61605129, 61635007, 61675137); Natural Science Foundation of Guangdong Province (2014A030308007, 2015B010105007, 2017A010102015); Education Department of Guangdong Province (2015KTSCX119); Science and Technology Innovation Commission of Shenzhen (JCYJ20160427104925452, JCYJ20170412105604705).

REFERENCES

1. Y. Yan, G. Xie, M. P. Lavery, H. Huang, N. Ahmed, C. Bao, Y. Ren, Y. Cao, L. Li, Z. Zhao, A. F. Molisch, M. Tur, and M. J. Padgett, Nat. Commun. **5**, 4876 (2014).
2. D. Grier, Nature **424**, 810 (2003).
3. R. Paez-Lopez, U. Ruiz, V. Arrizon, and R. Ramos-Garcia, Opt. Lett. **41**, 4138 (2016).
4. M. J. Padgett and L. Allen, J. Opt. B **4**, S17 (2002).
5. P. Gregg, P. Kristensen, and S. Ramachandran, Optica **2**, 267 (2015).
6. X. Cai, J. Wang, M. J. Strain, B. Johnson-Morris, J. Zhu, M. Sorel, J. L. O'Brien, M. G. Thompson, and S. Yu, Science **338**, 363 (2012).
7. Z. Zhao, J. Wang, S. Li, and A. E. Willner, Opt. Lett. **38**, 932 (2013).
8. C. Fu, S. Liu, Z. Bai, J. He, C. Liao, Y. Wang, Z. Li, Y. Zhang, K. Yang, B. Yu, and Y. Wang, J. Lightwave Technol. **36**, 1683 (2018).
9. W. Zhang, K. Wei, L. Huang, D. Mao, B. Jiang, F. Gao, G. Zhang, T. Mei, and J. Zhao, Opt. Express **24**, 19278 (2016).
10. S. Li, Q. Mo, X. Hu, C. Du, and J. Wang, Opt. Lett. **40**, 4376 (2015).
11. Y. Jiang, G. Ren, Y. Lian, B. Zhu, and W. Jin, Opt. Lett. **41**, 3535 (2016).
12. H. Wu, S. Gao, B. Huang, Y. Feng, X. Huang, W. Liu, and Z. Li, Opt. Lett. **42**, 5210 (2017).
13. Y. Zhao, Y. Liu, C. Zhang, L. Zhang, G. Zheng, C. Mou, J. Wen, and T. Wang, Opt. Lett. **42**, 4708 (2017).
14. Y. Han, Y. Liu, Z. Wang, W. Huang, L. Chen, H. Zhang, and K. Yang, Nanophotonics **7**, 287 (2018).
15. W. Zhang, L. Huang, K. Wei, P. Li, B. Jiang, D. Mao, F. Gao, T. Mei, G. Zhang, and J. Zhao, Opt. Lett. **41**, 5082 (2016).
16. G. K. L. Wong, M. S. Kang, H. W. Lee, F. Biancalana, C. Conti, T. Weiss, and P. St.J. Russell, Science **337**, 446 (2012).
17. X. Xi, G. K. L. Wong, M. H. Frosz, F. Babic, G. Ahmed, X. Jiang, T. G. Euser, and P. St.J. Russell, Optica **1**, 165 (2014).
18. Y. Zhang, F. Pang, H. Liu, X. Jin, S. Huang, Y. Li, J. Wen, Z. Chen, M. Wang, and T. Wang, IEEE Photon. J. **9**, 7101609 (2017).
19. H. Zhang, W. Zhang, L. Xi, X. Tang, X. Zhang, and X. Zhang, IEEE Photon. Technol. Lett. **28**, 1426 (2016).
20. T. Erdogan, J. Lightwave Technol. **15**, 1277 (1997).
21. Y. Wang, Y. Rao, Z. Ran, and T. Zhu, IEEE Photon. Technol. Lett. **15**, 251 (2003).
22. X. Xi, "Helically twisted solid-core photonic crystal fiber," Ph.D. dissertation (Max Planck Institute for the Science of Light, 2015).
23. H. Xu and L. Yang, Opt. Lett. **38**, 1978 (2013).
24. V. Kopp, V. Churikov, J. Singer, N. Chao, D. Neugroschl, and A. Genack, Science **305**, 74 (2004).